



SEPTEMBER 27 2023

Directional characteristics of two gamelan gongs

Samuel D. Bellows  ; Dallin T. Harwood; Kent L. Gee  ; Micah R. Shepherd



J. Acoust. Soc. Am. 154, 1921–1931 (2023)

<https://doi.org/10.1121/10.0021055>



CrossMark

Related Content

Low-frequency directional characteristics of a gamelan gong

Proc. Mtgs. Acoust. (March 2023)

Acoustic and vibrometry analysis of beating in a large Balinese gamelan gong.

J Acoust Soc Am (April 2009)

Acoustical and vibrometry analysis of a large Balinese gamelan gong

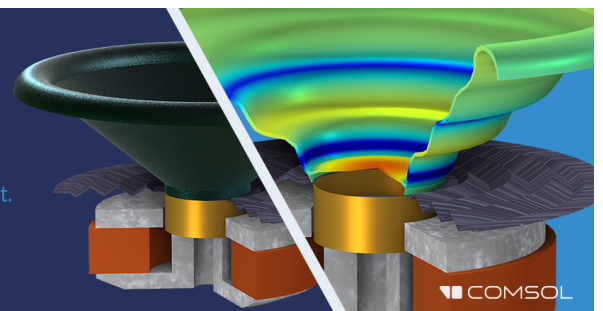
J. Acoust. Soc. Am. (June 2010)

01 October 2023 17:24:32

Take the Lead in Acoustics



The ability to account for coupled physics phenomena lets you predict, optimize, and virtually test a design under real-world conditions – even before a first prototype is built.

» Learn more about COMSOL Multiphysics®



COMSOL

Directional characteristics of two gamelan gongs

Samuel D. Bellows,^{a)}  Dallin T. Harwood, Kent L. Gee,  and Micah R. Shepherd

Acoustics Research Group, Brigham Young University, Provo, Utah 84006, USA

ABSTRACT:

The distinctive geometry and structural characteristics of Balinese gamelan gongs lead to the instrument's unique sound and musical style. This work presents high-resolution directivity measurements of two types of gamelan gongs to quantify and better understand their acoustic behavior. The measured instruments' structural modes clearly impact their far-field directivity patterns, with the number of directional lobes corresponding to the associated structural mode shapes. Many of the lowest modes produce dipole-like radiation, with the dipole moment determined by the positions of the nodal and antinodal regions. Higher modes exhibit more complex patterns with multiple lobes often correlated with the location and number of antinodal regions on the gong's edge. Directivity indices correspond to dipole radiation at low frequencies and quadrupole radiation at intermediate and higher frequencies. Symmetry analysis confirms that the gong's rim significantly impacts the resultant directivity.

© 2023 Acoustical Society of America. <https://doi.org/10.1121/10.0021055>

(Received 18 April 2023; revised 23 August 2023; accepted 25 August 2023; published online 27 September 2023)

[Editor: Andrew Morrison]

Pages: 1921–1931

I. INTRODUCTION

Sound radiation from musical instruments is an essential aspect of their unique sound and musical style. It also contributes to how an instrument portrays musical culture and tradition. Measured directivity patterns, a valuable tool in characterizing sound radiation, have numerous applications such as in room and concert hall acoustical designs,^{1,2} auralizations,^{3,4} and microphone placements.^{5,6} Previous directivity research has largely concentrated on Western orchestral instruments^{1,7–10} although there are notable exceptions.^{2,11,12} Nonetheless, many musical instruments with unique acoustic features, such as Indonesian gamelan gongs, have unresolved radiation characteristics.

Gamelan gongs, primarily found in the Bali and Java regions of Indonesia, are an essential part of the gamelan ensemble of percussion instruments, reflecting the region's rich and complex culture. Several types of gamelan gongs exist. The *gong ageng*, which translates to “large gongs” or “great gongs,” is the lowest pitch and comes in two variants: *lanang* (male) and *wadon* (female). The *wadon* and *lanang* gong ageng are struck with soft mallets on strong beats in Balinese gamelan music and are left to ring during musical transitions. Several smaller gongs also exist in the gamelan ensemble and have different musical purposes than the gong ageng. For example, the *kempur* is played with a soft mallet but is a higher pitch than the ageng, while the *bebende* is played with a small wooden hammer and is used for syncopation on off-beats. All are hand-made (traditionally from bronze) and therefore have non-constant thickness. Gamelan gongs differ from other gongs in that the edge of the rim is extended, wrapping backward a distance roughly equal to

half the radius of the gong. Gamelan gongs also have a raised dome (polished gold color) called a *boss* in their center. The height and size of the boss vary between the gamelan gong types.

The structural acoustics of gamelan gongs have been the focus of several studies. McLachlan¹³ measured changes in the acoustic outputs of gongs constructed of different materials due to his interest in the gong's tuning procedure. His results determined that the boss beaten into the gong's face raised its fundamental frequency, whereas thinning lowered it. His finite-element method (FEM) models illustrated how the boss shape, gong rim thickness, and rim angle all modified and tuned modal frequencies.

Varsányi¹⁴ further studied the unique acoustical features of Javanese gongs. Scanning laser Doppler vibrometer (SLDV) measurements provided details on the mode shapes, frequencies, and ordering of a gong ageng. Spectrograms of the acoustic signals produced by several gongs, including the gong ageng, *kempur*, and *gedè*, also aided in transient analysis of the identified modes. Fleischer and Fastl¹⁵ built upon this work by including a more detailed analysis of two Javanese gongs and nine Burmese gongs. Their results included extracted modal parameters from SLDV scans including mode shapes and relative frequencies as well as comparisons to a FEM model.

Krueger *et al.*^{16,18} investigated *ombak*,¹⁸ an acoustic beating phenomenon of the *wadon* gong ageng that occurs when struck on the boss. Microphone and SLDV measurements helped identify the natural frequencies of the instrument. In addition to determining the frequencies of the first two axisymmetric modes, they found frequency peaks at the second and third harmonics of the first mode, suggesting that non-linear effects exist. Other peaks at sum and difference frequencies of these modes were also detected. Subsequent

^{a)}Electronic mail: samuel.bellows11@gmail.com

measurements using increasing excitation force confirmed that nonlinear interactions occurred and were responsible for creating the ombak effect. Fleischer and Fastl¹⁷ studied the nonlinearity of several Burmese gongs and found similar results.

Perrin *et al.*¹⁹ studied a small gamelan gong. Their analysis employed finite-element method (FEM) modeling, electronic speckle pattern interferometry (ESPI), and SLDV scans to tabulate its modal frequencies. Although discrepancies in the modal frequencies arose between the measurement modalities, the authors generally found that the “modified Chladni’s law” gave predictions in good agreement with the ESPI data. They confirmed nonlinear behavior and identified three modes as the most acoustically significant: the radial (0, 1) mode and the pair of angular-radial (1, 1) modes.

While many studies have thus provided more knowledge regarding the structural modes of gamelan gongs, their acoustic radiation patterns have remained unclear. Zotter¹¹ measured the directivity of an ageng gamelan gong using a 10-channel microphone array and assuming axial symmetry. He found dipole-like directivity for the first two axial modes of the instrument. He also included results for time-varying directivities due to beating effects. However, the work only presented results for these first two modes and was further limited by the symmetry assumption.

This work compares the directivity patterns of an ageng lanang and a bebende Balinese gamelan gong evaluated by a high-resolution fully spherical directivity measurement system. Driving the gongs at low amplitude by a shaker ensured that nonlinear effects such as *ombak* did not occur. Subsequent SLDV scans accompany the directivity results and reveal connections between the gong’s far-field radiated patterns and its mode shapes. The results show that differences in the radiation patterns occur between the gongs for similar surface velocity distributions. Comparisons between computed directivity index (DI) values at resonance peaks to those of dipole and quadrupole sources highlight the gongs’ multidirectional radiation. Similar to Zotter’s results, the directivities show dipole-like radiation for the first two modes. Other low-order modes exhibit dipole-like radiation, while higher-order modes radiate with more complex directivity patterns. The sound power of each gong illustrates how structural mode ordering may relate to the musical purpose of the two gongs.

II. METHODS

A. Measurements

Figure 1 shows the lanang gong within the measurement system, whereas Fig. 2 shows the bebende gong. Both gongs are hand-made from bronze, with a thickness ranging from 2 to 4 mm. The radius of the lanang’s face is about 41 cm, while the radius of the bebende’s face is about 25 cm. In contrast to typical Javanese gongs, only the gong’s boss is polished to a gold color. While the lanang’s boss is pronounced, with a height of about 4 cm and a radius of

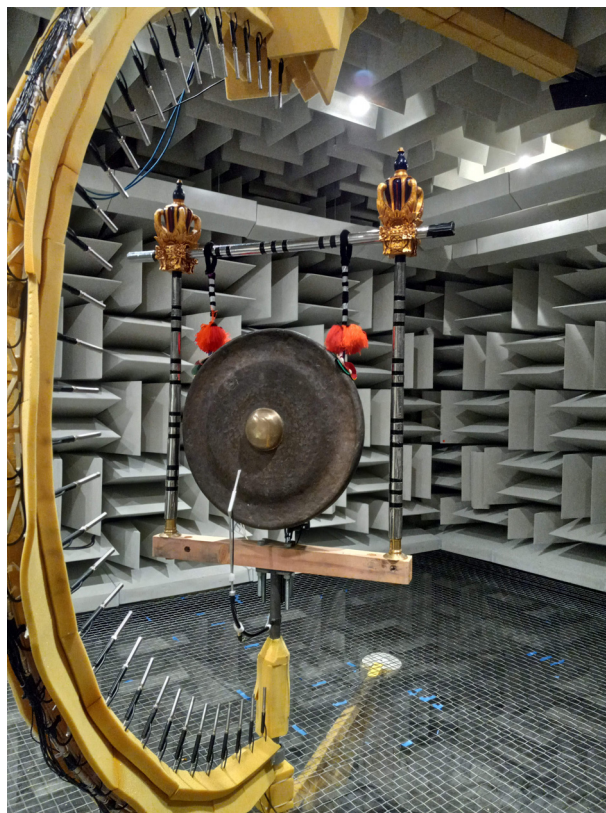


FIG. 1. (Color online) An ageng lanang gamelan gong within the rotating directivity measurement array.

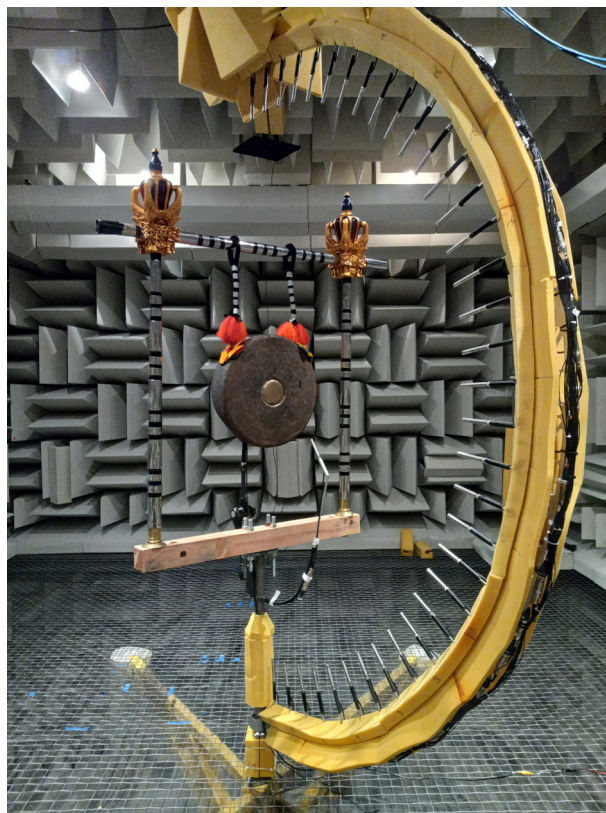


FIG. 2. (Color online) A bebende gamelan gong within the rotating directivity measurement array.

8.5 cm, the bebende’s 6 cm radius boss is sunken to a height of 0.3 cm. The sides extend backwards 24 cm for the lanang and 17.5 cm for the bebende. These elongated sides form a circular cavity behind the gong about 35 cm in radius for the lanang and 20.5 cm in radius for the bebende. This unique geometry due to the boss and elongated sides is less common, found primarily in Indonesia.

A rotating semicircular microphone array measured the directivity of the gamelan gongs. The microphone array consisted of 36 12.7 mm (0.5 in) precision microphones spaced in 5° increments in the polar angle. Array rotations in 5° azimuthal steps allowed a full spherical scan of 2521 unique sampling positions, consistent with the AES directivity sampling standard,²⁰ with the omission of the nadir position. A near-field reference microphone provided an acoustic input signal for calculating frequency response functions (FRFs) between it and the output of each array microphone signal. Frequency-dependent relative calibrations between the array and reference microphones ensured proper level normalizations in subsequent post-processing which would otherwise appear as latitudinal banding in directivity balloon plots.⁹

Three repetitions of a 5 s linear swept-sine input signal sent to a shaker (LDS V203) excited the gong over the audible bandwidth. Although the large gamelan gong’s have interesting non-linear vibrations, this work applied low-amplitude levels to ensure operation over the linear regime of the gong. A small moveable mount positioned the shaker behind the gong, allowing several measurements with different contact points. The contact position used in the following analysis was placed on the back side of the gong’s face between the boss and rim wall, as this position excited several modes which do not appear when the shaker attached directly to the gong’s boss. Each of the 72 azimuthal positions produced 37 24-bit, 48 kHz recordings using Focusrite Rednet4 digital audio interfaces.

The structural vibrations of the gong determine its directional behavior. Thus, visualizations of the gongs’ surface velocity provide insight into the gong’s directivity. To better understand how the gong’s modal shapes influenced its directivity, additional measurements followed from an SLDV scan of the instruments. Similar to the directivity measurements, the shaker excited the instrument while the SLDV laser head scanned 977 positions on the gong’s front face. The shaker’s position was in a similar location so that all measured modes of interest appeared in both the SLDV scan and directivity results. The spatial resolution allowed modal analysis well above 1.5 kHz, although this work primarily focuses on results up to this frequency.

B. Signal processing

While the shaker input excitation signal is more repeatable than that of played musical instruments, FRFs nonetheless increase extraneous noise immunity and provide a convenient normalization to address any variations that might occur between measurement rotations.⁹ The FRF H_{uv}

for the u th array microphone and the v th rotation is defined as^{21–23}

$$H_{uv}(f) = \frac{G_{ab,uv}(f)}{G_{aa,v}(f)}, \tag{1}$$

where $G_{ab,uv}$ is the cross-spectrum between the array microphone signal and the near-field reference microphone signal and $G_{aa,v}$ is the autospectrum of the near-field reference microphone signal.

The radiated sound power of the source provides a straightforward method to identify the gong’s modal frequencies. Because a spherical surface followed from multiple rotations of the measurement system, the time-averaged sound power radiated by the gong was^{21,26}

$$\langle W(f) \rangle_t = \frac{R^2}{\rho_0 c} \sum_{u=0}^{U-1} \sum_{v=0}^{V-1} w_{uv} G_{aa,v}(f) |H_{uv}(f)|^2, \tag{2}$$

where w_{uv} are quadrature weights for numerical integration over the sphere^{24,25} for the $U = 36$ microphones and $V = 72$ rotations, R is the measurement radius, and the subscript t indicates time-averaging over the excitation (swept-sine) signal length. Peaks of $\langle W(f) \rangle_t$ indicated the gong’s modal frequencies for further analysis.

Coherence functions at each sampling position γ_{uv}^2 also helped quantify noise levels and indicated when the instrument excitation levels were no longer sufficient to produce meaningful directivity functions.²³ The spatially averaged coherence follows by averaging the coherence function over the sphere,

$$\langle \gamma^2(f) \rangle_S = \sum_{u=0}^{U-1} \sum_{v=0}^{V-1} w_{uv} \gamma_{uv}^2(f). \tag{3}$$

It provides a useful metric for evaluating the signal-to-noise ratio over the entire measurement surface for a particular frequency. The averaged value over all modes considered was $\langle \gamma^2(f) \rangle_S = 0.97$, indicating acceptable signal-to-noise ratios over the frequencies of interest.

C. Spherical harmonics and directivity functions

The spherical harmonics provide an orthonormal basis for expanding directivities over the spherical evaluation surface.^{11,27} As the angular component of the Helmholtz-equation solution on the exterior domain, they find important applications in wave-based modeling of sound fields.²⁸ The normalized spherical harmonics of degree n and order m are defined here as²⁹

$$Y_n^m(\theta, \phi) = \sqrt{\frac{2n+1}{4\pi} \frac{(n-m)!}{(n+m)!}} P_n^m(\cos \theta) e^{im\phi}, \tag{4}$$

where P_n^m are the associated Legendre functions of degree n and order m .

The pressure field for $r \geq R$ is²⁸

$$p(r, \theta, \phi, k) = \sum_{n=0}^{\infty} \sum_{m=-n}^n c_n^m(k) h_n^{(2)}(kr) Y_n^m(\theta, \phi), \quad r \geq R, \quad (5)$$

where $h_n^{(2)}(kr)$ are the spherical Hankel functions of the second kind (for outward propagation and $e^{i\omega t}$ time dependence). The expansion coefficients follow by exploiting the spherical harmonic's orthogonality over the sphere:

$$c_n^m(k) = \frac{1}{h_n^{(2)}(kR)} \int_0^{2\pi} \int_0^{\pi} p(R, \theta, \phi, k) [Y_n^m(\theta, \phi)]^* \sin \theta d\theta d\phi, \quad (6)$$

where an asterisk indicates complex conjugation. Numerical quadrature allows evaluation of the integral, with the spatial sampling density permitting converging expansions up to a maximum $N=34$ degree expansion.^{24,25,27}

Because the measurement system produces discretely sampled directivity functions, considering the frequency range under which the sampling density remains sufficient for analysis is important. For spherical-harmonic-based applications, spatial aliasing effects may limit the usable frequency bandwidth. One approach to identifying spatial aliasing is to consider the magnitude of the spherical harmonic coefficients of a given degree. Because the maximum degree n necessary for representation at a given wavenumber k is roughly $n=ka$, where a is the source dimension, one may estimate an initial limiting frequency based on geometric arguments.³⁰ For example, the ageng lanang gong radius is $a=0.41$ m so that a maximal spherical harmonic expansion degree of $N=34$ suggests an upper bound of around 4.5 kHz.

A more complete picture follows by plotting a source's spherical spectrum. The energy per degree metric²⁷

$$E_n(k) = \sum_{m=-n}^n |c_n^m(k)|^2 \quad (7)$$

represents the signal energy contained across all spherical harmonic orders m for the same degree n . Figure 3 plots the spherical spectrum²⁸ based on this metric for the larger ageng lanang gong over expansion degree n and frequency f . Color indicates the level of each coefficient relative to the maximum for each frequency on a logarithmic scale. White indicates high energy (important) coefficients whereas black indicates low energy (unimportant) coefficients. As anticipated, the number of expansion coefficients required increases linearly with respect to frequency. The overlaid dashed line indicates the line $n = (0.41 \text{ m})k$, based on geometrical arguments. The regions of coefficients with the largest magnitudes fall below this line. However, it is also apparent that there are some coefficients above this line which are non-negligible. Ensuring that the expansion has all coefficients with no less than -20 dB down from the maximum limits the maximum frequency range to about 2 kHz. This limiting frequency lies above the frequencies

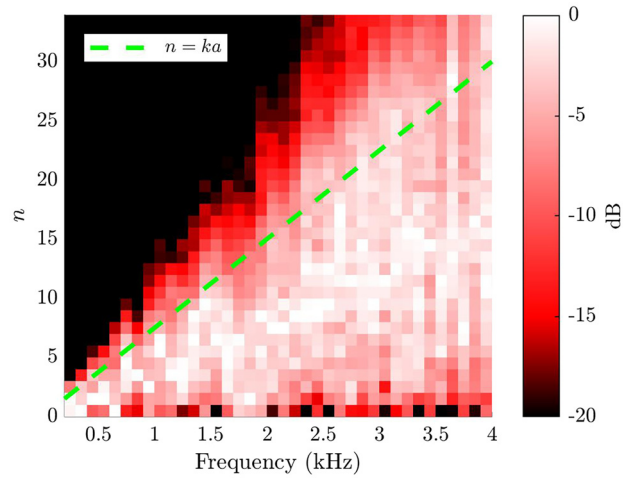


FIG. 3. (Color online) Spherical spectrum of the ageng lanang gamelan gong. Each rectangle indicates the energy contained in a given expansion coefficient summed over all orders m for fixed degree n calculated in 100 Hz steps.

under analysis in the present work so that the spatial sampling resolution is sufficient. Because the bebende gong is smaller than the ageng lanang, aliasing effects do not occur until an even higher frequency.

Once determined, the expansion coefficients allow computation of extrapolated far-field directivities via the large-argument representations of the spherical Hankel functions²⁶

$$D(\theta, \phi, f) = \sum_{n=0}^N \sum_{m=-n}^n c_n^m(k) i^{n+1} Y_n^m(\theta, \phi), \quad (8)$$

where N is the maximum spherical harmonic degree used ($N=34$ in the present work) and i is the imaginary unit. Extrapolation of the complex pressure also allows far-field corrections for the sound power estimate when R is in the near-field of the source. Additionally, far-field propagation corrects near-field directivity variations due to possible source misalignment between the acoustic center of the source and the geometric center of the array.^{31,32}

The directivity factor function, defined as³³

$$Q(\theta, \phi, f) = \frac{4\pi |D(\theta, \phi, f)|^2}{\int_0^{2\pi} \int_0^{\pi} |D(\theta', \phi', f)|^2 \sin \theta' d\theta' d\phi'}, \quad (9)$$

represents the sound intensity in a given direction relative to the that of an omnidirectional source with the same sound power. Although the directivity factor function is often defined in the direction of a source's principle axis of radiation, it is convenient to extend this definition to arbitrary angles for sources whose direction of strongest radiation varies over frequency such as gongs (see Sec. IV B). The directivity index DI expresses the directivity factor function on a logarithmic scale, i.e., $DI = 10 \log_{10} Q$.

A directivity factor function deviation σ_Q quantifies directivity deviations between two different patterns as³⁴

$$\sigma_Q = \int_0^{2\pi} \int_0^\pi |Q_1(\theta, \phi) - Q_2(\theta, \phi)| \sin \theta d\theta d\phi. \quad (10)$$

It may be expressed on a logarithmic scale as

$$L_Q = 10 \log_{10}(1 + \sigma_Q), \quad (11)$$

where the addition of one maps a value of $\sigma_Q = 0$ to a deviation level $L_Q = 0$ dB. It is similar to the area-weighted root mean square deviation²³ except for directivity normalization by power instead of levels.

III. RESULTS

A. Directivity results

1. Ageng lanang

Figures 4(a)–4(e) shows the propagated far-field directivities [Eq. (8)] at frequencies corresponding to the lowest five modal peaks. Color and balloon radius indicate the relative levels on a 40 dB scale and the overlaid grid indicates the angular locations of the sampling positions of the measurement system. The gong faced the 0° azimuthal angle marker during the measurements. All directivity balloons appear from the same vantage point, above and slightly to the left of the gong. Figures 4(f)–4(j) plots the out-of-plane surface velocities as measured by the SLDV. The velocities are normalized to the maximum with red color indicating in-phase vibrations and blue indicating out-of-phase vibrations.

As seen in Figs. 4(a)–4(c), the directivity is roughly dipolar for the first three modes. At 63 Hz [Fig. 4(a)], the dipole moment falls to the x -direction (towards the 0° azimuthal marker) so that a null occurs in the plane of the gong face (yz -plane). However, for the other two frequencies, the dipole moment is directed towards the positive y - z -direction at 94 Hz [Fig. 4(b)] and the negative y - z -direction for 104 Hz [Fig. 4(c)]. These latter two modes appear to be roughly variations of each other through a 90° rotation.

Visualization of the associated surface velocity provides some insights into the directional behavior. For example, at 63 Hz [Fig. 4(f)], the gong appears to be vibrating as a (0, 1) mode. Consequently, the gong’s face moves forwards and backwards along the x axis. This vibration is similar to that of an oscillating disk which produces a dipole-like directivity.²⁶ Thus, the dipole-like directivity seen in Fig. 4(a) may be attributed to this motion.

Figures 4(g) and 4(h) show (1, 1) modal patterns. Although the mode shapes appear visually as rotated variations of each other, the SLDV scan and sound power peaks indicate a 10 Hz separation (see Fig. 8) so that the mode is not degenerate. This is discussed further in Sec. V but is consistent with the results from multiple gongs of various sizes and styles.¹⁴ Interestingly, the null lines in the dipole-radiation seen in Figs. 4(b) and 4(c) align with the apparent node lines on the gong’s surface.

At 130 Hz [Fig. 4(d)], the directivity is bi-directional, with the strongest radiation in front of and behind the gong. Although the pattern is somewhat similar to that of the dipole-like radiation at 63 Hz, the null between the two strongly radiating lobes is not as pronounced. At 63 Hz, the null is nearly 20 dB down from the maximum compared to only about 10 dB down at 130 Hz. The corresponding surface velocity [Fig. 4(i)] shows a (0, 2) mode. Interestingly, these axisymmetric (0, 1) and (0, 2) modes at 63 and 130 Hz share quasi-axisymmetric radiation patterns.

The directivity at 168 Hz [Fig. 4(e)] is more complex, with strong radiation in a broad region in front with reduced radiation behind the gong. Its associated surface velocity [Fig. 4(j)] shows four regions of in and out-of-phase vibration which appear as a distorted (2, 1) pattern. Unlike for the other modes, there does not visually appear to be a direct correlation between surface null lines and the radiated pattern.

Figure 5 plots the directivity for select higher frequency modal peaks. While at lower frequencies the radiation is simpler and primarily dipolar for many modes, the directivity at higher frequencies becomes more complex. For example, at

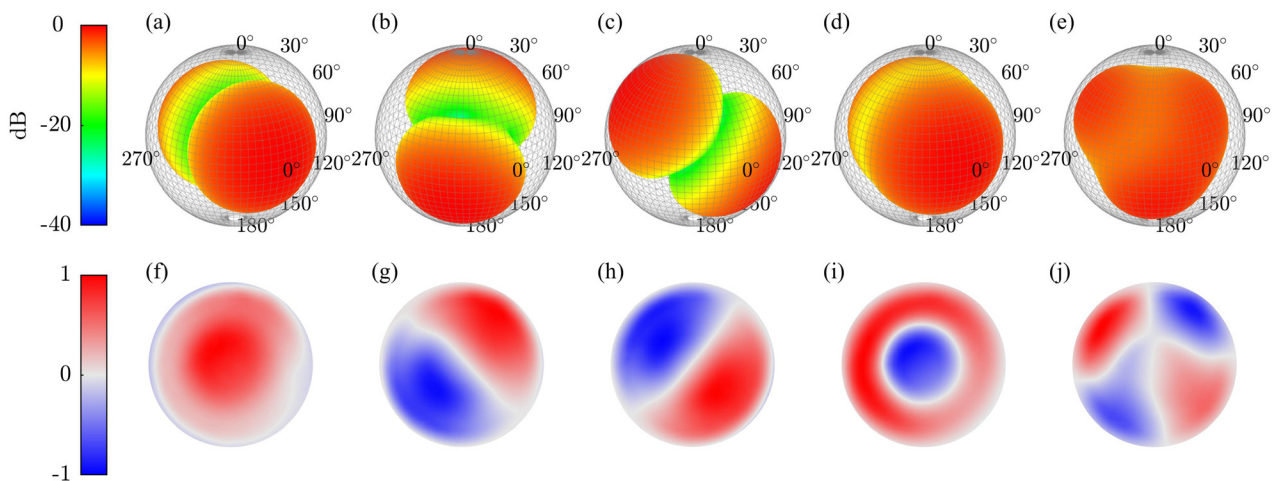


FIG. 4. (Color online) Propagated far-field directivities [Eq. (8)] for the ageng lanang’s lowest five modal frequencies. (a) 63 Hz, (b) 94 Hz, (c) 104 Hz, (d) 130 Hz, (e) 168 Hz. Out-of-plane surface velocity for the same modal frequencies. (f) 63 Hz, (g) 94 Hz, (h) 104 Hz, (i) 130 Hz, (j) 168 Hz.

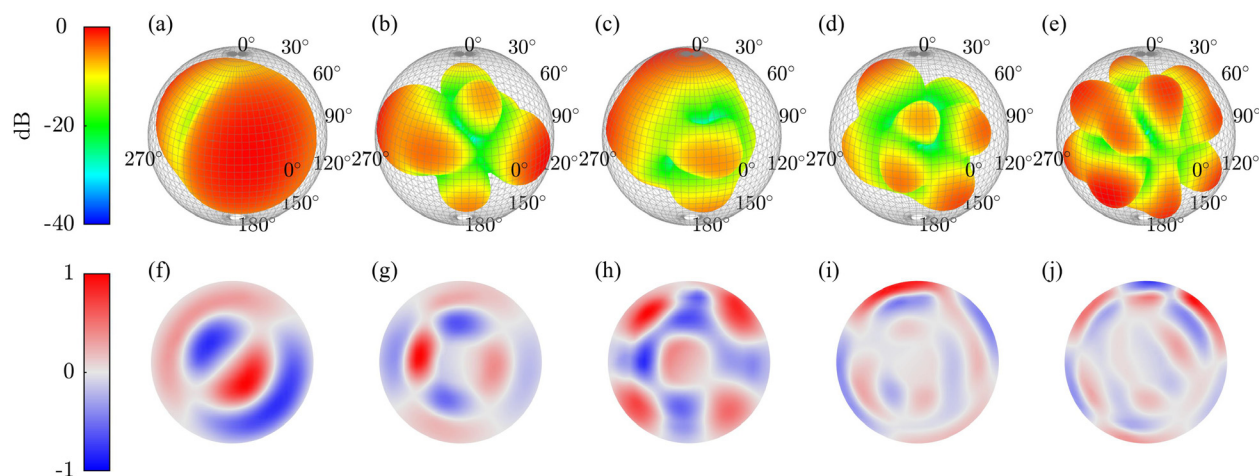


FIG. 5. (Color online) Propagated far-field directivities [Eq. (8)] for select higher frequency modes of the lanang ageng. (a) 198 Hz, (b) 376 Hz, (c) 420 Hz, (d) 566 Hz, (e) 650 Hz. Out-of-plane surface velocity for the same modal frequencies. (f) 198 Hz, (g) 376 Hz, (h) 420 Hz, (i) 566 Hz, (j) 650 Hz.

367 Hz [Fig. 5(b)], the directivity pattern has four distinct lobes directed to the sides of the gong. The two lobes closest to the transverse (xy) plane are about 5 dB stronger than those falling along the median plane. Some slight radiation is also apparent behind the gong. The associated surface velocity [Fig. 5(g)] appears as a (2, 2) mode with one radial node line and two angular node lines, leading to eight regions of in and out-of-phase vibration. The location of the angular node lines agrees with the location of the directivity nulls seen in Fig. 5(b) in a similar fashion to the dipole-like results at 94 and 104 Hz [Figs. 4(b) and 4(c)].

In contrast, at 420 Hz [Fig. 5(c)] the radiation is primarily behind the gong and relatively little sound radiates to the sides. The surface velocity at 420 Hz [Fig. 5(h)] is more complex and does not appear to have a direct correspondence to the directional response. Figure 5(d) reveals that eight lobes which are roughly uniformly distributed around the gong form at 566 Hz. Interestingly, the radiation lobes behind the gong are stronger than those in front by about 3 dB. Despite its complex surface velocity distribution [Fig. 5(i)], there are four edge anti-nodal regions, which appear to correspond to the nulls between directional lobes in the radiated pattern.

At 650 Hz [Fig. 5(e)], a quasi-symmetric six-lobed pattern forms, with the strongest regions of radiation being to the sides of the gong. Again, six edge anti-nodal regions appear [Fig. 5(j)] and tend to align with the location of nulls between the directivity lobes. Although the radiated sound power for these modes is less significant compared to the lower-frequency modes (see Sec. IV A), these few examples illustrate the complexity of the gong's radiation at higher frequencies. Additionally, the correspondence between edge anti-nodal regions and the number of directivity lobes forming at 94, 104, 420, 566, and 650 Hz strongly suggests their significant role in gamelan gong radiation.

2. Bebende

The bebende gong shows some similarities to the larger ageng lanang gong, although distinct differences remain.

Figure 6 plots the directivity of the lowest five measured modal frequencies of the bebende gong. Similar to previous figures, the out-of-plane surface velocity for the same frequencies appear below for reference. Like the ageng lanang, the lowest mode at 144 Hz [Fig. 6(a)] corresponds to a dipole-like directivity, with the dipole moment on-axis and the null appearing in the plane of the gong. Both these modes correspond to a similar (0, 1) mode-like surface velocity [Figs. 4(f) and 6(f)].

However, the next two modes present different directional characteristics than those corresponding to the same mode shape for the ageng lanang. At 226 Hz [Fig. 6(b)] and 239 Hz [Fig. 6(c)], the directivity remains quasi-dipole like with the dipole moment oriented slightly up and down, respectively. However, the surface velocities, which both appear as (1, 1) modes in Figs. 6(g) and 6(h), are similar to those of the ageng lanang seen in Figs. 4(g) and 4(h). Despite the similarities of the surface velocity, the directivities appear very different.

The mode ordering between the ageng lanang and the bebende is the same for the first three modes. For the next three, the order differs, with the (1, 2) mode appearing before the (0, 2) mode for the bebende gong. The different ordering is seen in the directivity patterns. At 389 Hz [Fig. 6(d)], the directivity balloon has four lobes roughly corresponding to the four anti-nodal regions seen in the (1, 2) mode shape. At 469 Hz [Fig. 6(e)], the directivity appears more omnidirectional than that for the corresponding mode shape for the ageng lanang [Fig. 4(d)].

Higher frequency results shown in Fig. 7 highlight unique radiation characteristics for the bebende gong. Similar to the results for the ageng lanang, the location and number of anti-nodal regions on the gongs face correspond to the number of lobes to the side of the gong for the directivity at the modal peaks at 592 Hz [Fig. 7(a)], 849 Hz [Fig. 7(b)], and 1112 Hz [Fig. 7(c)]. The surface velocity distributions at these frequencies, seen in Figs. 7(f)–7(h), have two, four, and six anti-nodal edge regions which correspond to the location and position of the two, four, and six lobes seen

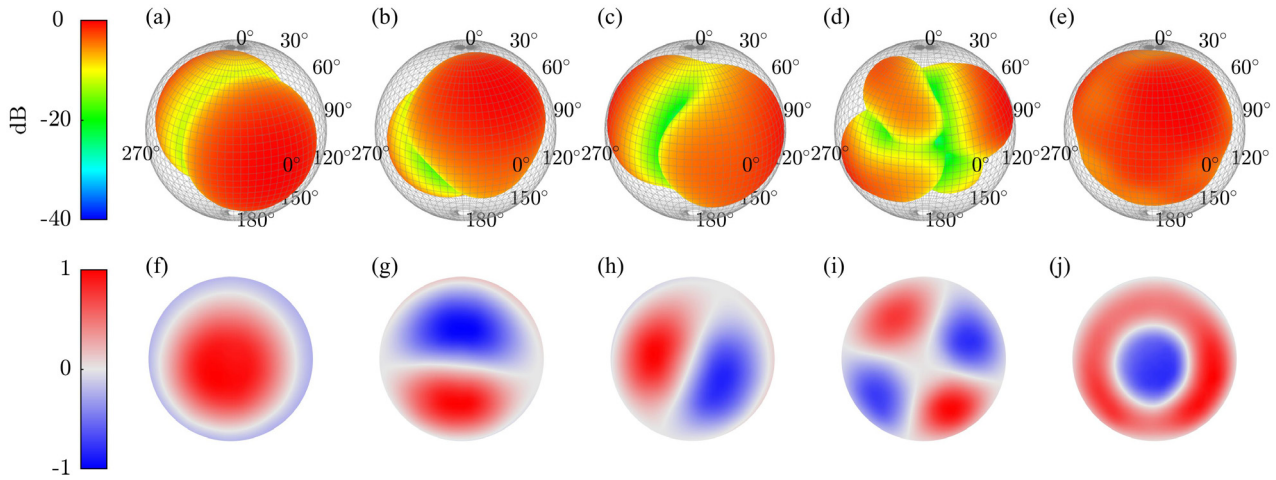


FIG. 6. (Color online) Propagated far-field directivities [Eq. (8)] for the bebende gong’s lowest five modal frequencies. (a) 144 Hz, (b) 226 Hz, (c) 239 Hz, (d) 389 Hz, (e) 469 Hz. Out-of-plane surface velocity for the same modal frequencies. (f) 144 Hz, (g) 226 Hz, (h) 239 Hz, (i) 389 Hz, (j) 469 Hz.

in Figs. 7(a)–7(c). Thus, similar to the ageng lanang, at higher frequencies the radiation appears to be influenced by the number and location of anti-nodal edge regions.

The directivity at 1180 Hz [Fig. 7(d)] and 1204 Hz [Fig. 7(e)] each have six lobes. Unlike those seen in Figs. 7(a)–7(c); however, the lobes do not fall in the plane of the gong’s face (yz plane). The associated normal particle velocity seen in Figs. 7(i)–7(j) show an apparent (1, 3) mode, leading to six anti-nodal regions. The orientation of these anti-nodal regions corresponds very strongly to the six lobes visible in the far-field radiated pattern.

IV. ANALYSIS

A. Modal frequencies

Despite belonging to the same instrument family, the directivity patterns of the ageng lanang and bebende gongs greatly differ even for similar surface velocities. These differences in part may be due to differing geometry and material inhomogeneity. For example, the ageng lanang has a

deeper boss and shallower side walls. However, another important characteristic is the acoustic wavelength relative to the structural modal frequency.

To consider these differences, Fig. 8 plots the normalized $\langle W(f) \rangle_t$ radiated by the ageng lanang gong when excited by the shaker, plotted as a function of both frequency dimensionless ka , where $a=0.41$ m is the gong’s radius. While this radiated power spectrum will differ from that produced by the gong when struck with a mallet, it does provide insight into the gong’s modal frequencies. Due to the nonlinear behavior of the gong, determining the radiated power of each mode as a function of striking force requires further analysis beyond the scope of this work. The sound power curve reveals that the instrument’s modal nature strongly characterizes its acoustic output. Below 200 Hz, eight sharp, distinct peaks evidence the gong’s lowest modes. The spectral region from 200 Hz to around 350 Hz appears as a gap with no strongly radiating modes. The spectral region between 350 Hz and 1 kHz shows increased modal density with many modes radiating within 20 dB

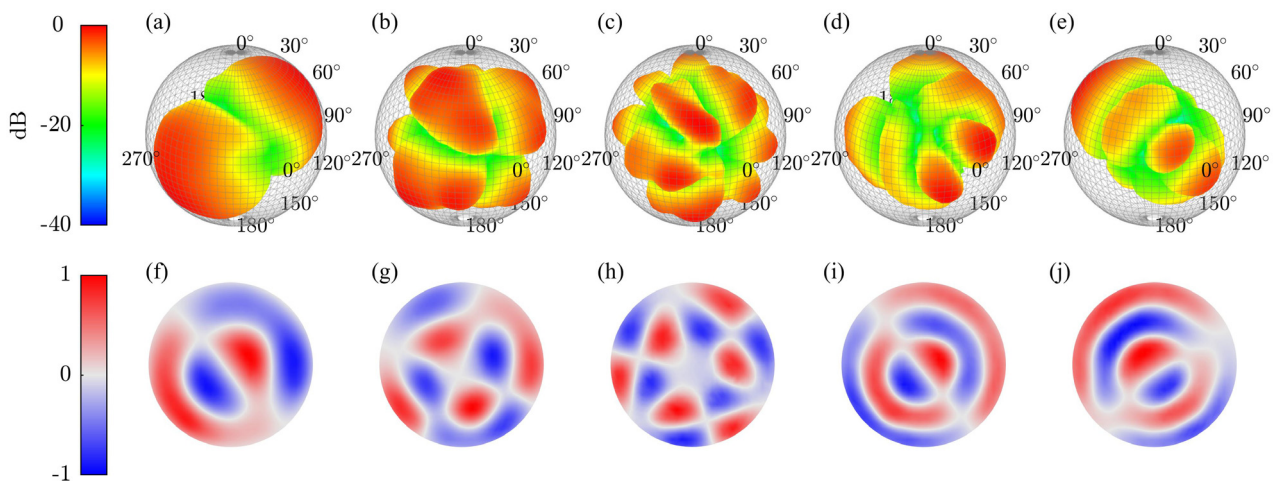


FIG. 7. (Color online) Propagated far-field directivities [Eq. (8)] for select higher frequency modes of the bebende. (a) 592 Hz, (b) 849 Hz, (c) 1112 Hz, (d) 1180 Hz, (e) 1204 Hz. Out-of-plane surface velocity for the same modal frequencies. (f) 592 Hz, (g) 849 Hz, (h) 1112 Hz, (i) 1180 Hz, (j) 1204 Hz.

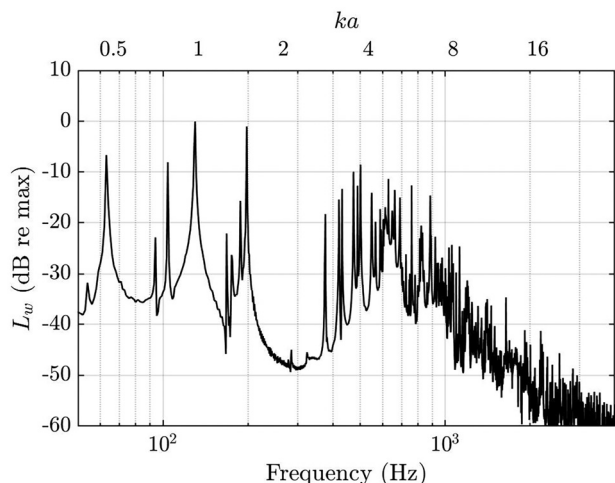


FIG. 8. Normalized time-averaged sound power spectrum radiated from the ageng lanang gong when excited by a shaker.

down from the maximum. Above 1 kHz, the radiated power rolls off at roughly 10 dB per octave.

Figure 9 plots the normalized $\langle W(f) \rangle_t$ radiated by the bebende gong when excited by the shaker, plotted as a function of both frequency dimensionless ka , where $a = 0.25$ m is the gong's radius. In contrast to the ageng lanang gong's result, there does not appear to be a bandgap between the lowest and higher modes. Additionally, the spacing between modal peaks and their relative wavelengths differ between the two gongs.

Tables I and II tabulate the modal frequencies, associated acoustic wavenumber, and estimated radial and angular node numbers for the first ten modes of the gongs. While the ordering of the first three modes is the same for both gongs, significant differences arise for the other higher modes. These ordering differences in turn lead to different acoustic wavelengths for the same mode number. Consequently, even if the gongs had similar sizes and geometry, the differing mode order relative to frequency would lead to distinct

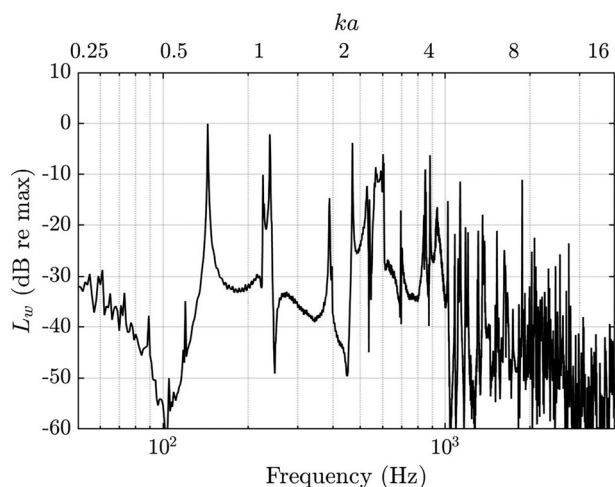


FIG. 9. Normalized time-averaged sound power spectrum radiated from the bebende gong when excited by a shaker.

TABLE I. Ageng lanang gong mode order based on SLDV measurements.

Frequency (Hz)	ka	Angular number	Radial number
64	0.5	0	1
94	0.7	1	1
104	0.8	1	1
130	1.0	0	2
168	1.3	2	1
174	1.3	2	1
188	1.4	1	2
198	1.5	1	2
276	2.1	3	1
284	2.1	3	1

directivity patterns. The observed modal frequencies also show that no truly degenerate modes appear, although modes with similar radial and angular numbers typically fall within 10 Hz of each other, such as the (1, 1), (2, 1), (1, 2), and (3, 1) modes of the ageng lanang and the (3, 1) mode of the bebende gong. These results are consistent with the modal analysis performed by Fleischer and Fastl,¹⁵ who likewise found slight frequency differences for the (1, 1) modes. This slight frequency separation of modes with similar shapes likely results from the hand-hammered construction of the gongs which breaks the material homogeneity.

In addition to variations in directivity patterns, differences in the gong's modal frequencies explains why the lanang produces ombak while the bebende does not. Krueger *et al.*¹⁶ determined that ombak occurs because non-linear excitation of the first axisymmetric mode generates a harmonic near the second axisymmetric mode. This second harmonic has also been observed by Varsányi,¹⁴ Fleischer and Fastl,¹⁷ and Zotter¹¹ and likely results from a geometric non-linearity induced by curvature in the instrument.⁴¹ For the lanang, the first axisymmetric mode (0, 1) appears at 64 Hz. Consequently, a non-linearly produced second harmonic would appear near 128 Hz. This is only slightly lower than the 130 Hz second axisymmetric mode (0, 2) and would lead to a 2 Hz beating when excited together. In contrast, the bebende's first axisymmetric mode resonates at 144 Hz so a non-linearly produced second harmonic would appear at 288 Hz. This frequency is not near the 472 Hz second axisymmetric mode nor any other measured modes. Thus,

TABLE II. Bebende gong mode order based on SLDV measurements.

Frequency (Hz)	ka	Angular number	Radial number
144	0.7	0	1
224	1.0	1	1
240	1.1	1	1
388	1.8	2	1
472	2.2	0	2
536	2.5	3	1
546	2.5	3	1
606	2.8	1	2
692	3.2	4	1
844	3.9	2	2

modal frequency location clarifies why the lanang produces a beating phenomena when strongly struck whereas the bebende does not.

B. Directivity index

The directivity index (DI) provides a simple metric for quantifying how directional a source is. It is typically reported as a value along the principal axis of radiation, although some have considered its generalization to the entire sphere.^{6,33} For loudspeakers and other transducers, the principal axis of radiation is usually obvious from source geometry. However, as evidenced by their complex, multi-directional radiation patterns, this is not the case for the gamelan gongs. To accommodate the complex radiation patterns of the gamelan gongs, this work extracts the maximum DI value over the sphere and its associated angular position similar to the approach applied in Ref. 35.

Figure 10(a) plots the maximum value of the DI over the sphere at each extracted modal peak. The relative marker size indicates relative frequency, so that lower frequency modes have smaller markers and higher frequency modes have larger markers. The DI values for the ageng lanang appear as circles whereas those for the bebende appear as diamonds. For a dipolar source, $D(\theta, \phi) \propto \cos \theta$ (Ref. 26) so the DI is $10 \log_{10} 3 \approx 4.77$ dB. This value is overlaid as a dashed line. The eight lowest modes of the ageng lanang and the lowest three modes and the fifth mode of the bebende fall into this range. This is in good agreement with

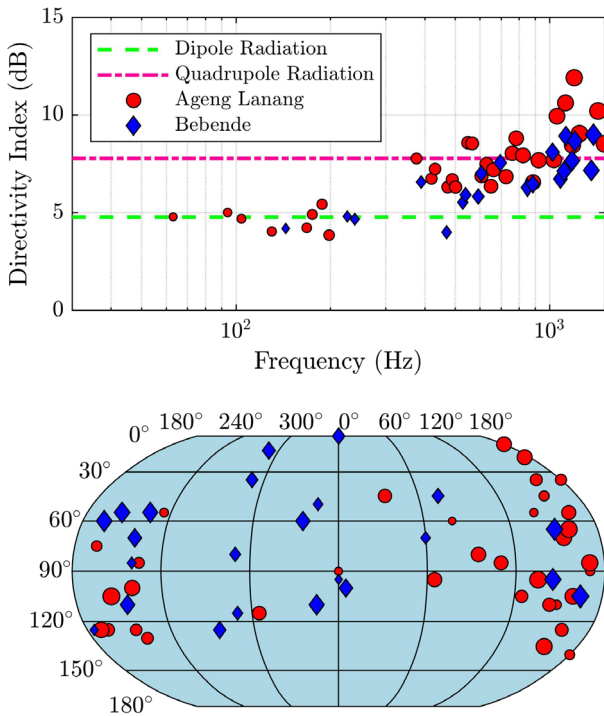


FIG. 10. (Color online) (a) Maximum DI over frequency. (b) Angular location of the direction of strongest radiation. The relative size of the marker indicates the relative frequency (i.e., a smaller marker is at a lower frequency).

the directivities seen in Figs. 4(a)–4(d) and Figs. 6(a)–6(c), which have dipole-like radiation characteristics.

For a lateral quadrupole, $D(\theta, \phi) \propto \cos \theta \cos \phi$ (Ref. 26) so the DI is $10 \log_{10} 6 \approx 7.78$ dB. This value is overlaid as a dash-dot line. From around 200 Hz to 1 kHz, the DI climbs from levels corresponding to dipole radiation to levels corresponding to quadrupole radiation. Above 1 kHz, the DI for some modes increases higher, approaching a level of 12 dB.

Figure 10(b) plots the direction of the strongest radiation over the sphere. Interestingly, the trends of both gongs is markedly different. For the ageng lanang, only a few modes (including the lowest) radiate strongest directly in front of the gong. Most of the other modes radiate strongly in the region $x < 0$ (behind the gong face’s plane). For the bebende gong, more modes tend to radiate strongly in region $x > 0$ (in front of the gong face’s plane) compared to the ageng lanang, although many also radiate strongly to the side and behind. These results are also in good agreement with the select directivities seen in Figs. 4–7.

Because of the noted correlations between edge antinodal regions and the number of lobes, it is insightful to consider the DI as a function of both angular and radial node number rather than frequency. Figure 11 plots the DI values as a function of the estimated angular and radial node numbers for the extracted modal frequencies. Although there are some trends, such as general lower DI values for

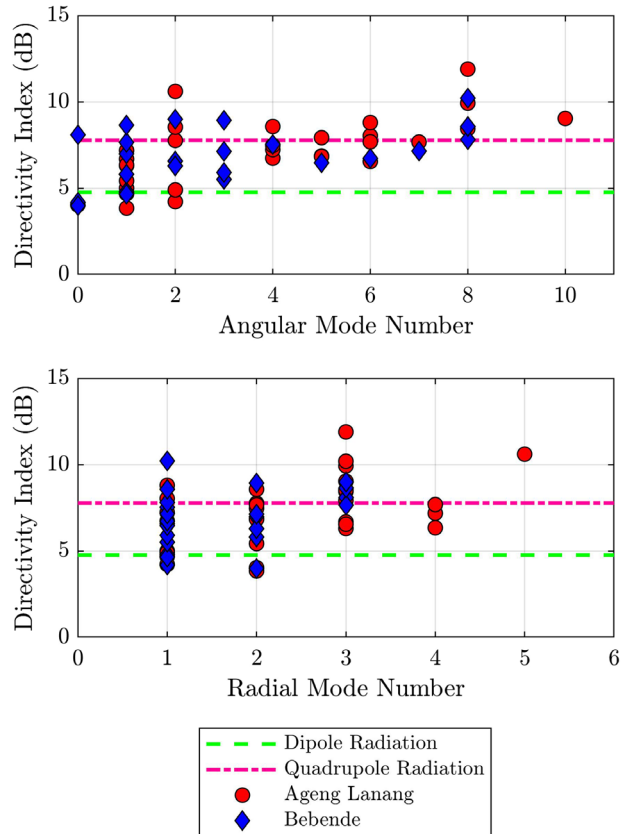


FIG. 11. (Color online) Directivity Index as a function of (a) angular node number (b) radial node number.

low angular node numbers, the spread of DI as a function of angular and radial node number is quite large. Nonetheless, it does appear, especially for angular numbers greater than 3, that the DI may be correlated to the number of angular node lines. Nonetheless, the inclusions of even higher modes than considered in this study could modify this trend.

The DI values and positions quantify radiation trends visualized in the directivity balloons. First, at low frequencies, the radiation is primarily dipole-like. For intermediate and higher frequencies it rises to levels similar and exceeding quadrupole-like radiation. Thus, the gongs can be considered multi-directional radiators. In general, the strongest regions of radiation for many modes are to the side and behind the gong. Last, angular node number may be more strongly correlated with DI values than radial node number.

C. Impact of side walls on median plane symmetry

If the gamelan gongs were flat plates with no sidewall, one would anticipate strong symmetries about the median plane of the gong. However, the measured radiation patterns clearly show that the addition of the side walls as well as other inhomogeneities in the hammered gongs influence their directivity, leading to deviations from anticipated reflectional symmetries. Symmetry analysis helps quantify these deviations from an idealized source with no side walls.

To consider deviations from symmetry, let Q_s be the symmetrized directivity function

$$Q_s(\theta, \phi) = \frac{1}{2}(Q(\theta, \phi) + Q_r(\theta, \phi)), \quad (12)$$

where Q is defined in Eq. (9) and Q_r is the reflected directivity factor function across the median plane. Q_s thus represents the average value between both planes. Figure 12 plots L_Q [Eq. (11)] between the symmetrized and measured data. Only for a handful of modes is the measured reflectional symmetry strong enough to avoid differences less than 1.0dB. Most modes fall into the range of 1 to 2 dB

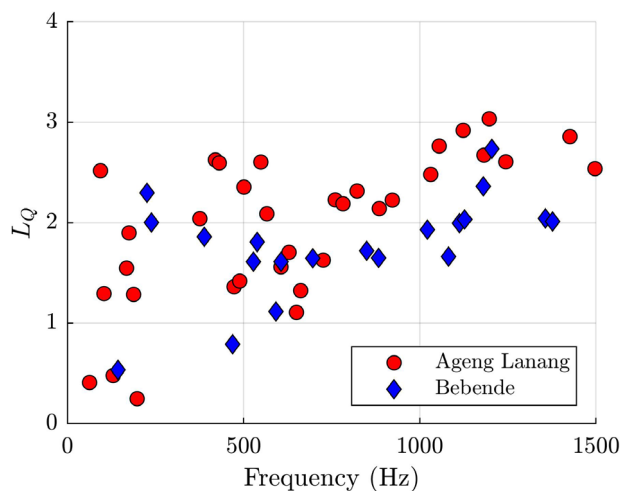


FIG. 12. (Color online) Deviations between measured and symmetrized data about the median plane.

difference between measured and symmetrized data, although some modes approach and exceed 3 dB. Thus, the unique geometry of the gongs leads to deviations from anticipated symmetries of other gongs and percussion instruments.

V. DISCUSSION

Sound radiation from gamelan gongs is complex. While at lower frequencies the radiation patterns are simple and dipole-like, higher modes develop complicated, multi-directional radiation. Often the number and location of edge anti-nodal regions correlates with the number of radiation lobes. Nonetheless, the unique construction and geometry of the gongs often leads to unanticipated directional behavior.

While somewhat similar in general shape, the ageng lanang and bebende gongs serve unique musical functions within the Balinese gamelan. As a result, the instruments' geometry and hand-tuned modal frequencies are distinctive to each instrument. These variations appear both in the ordering and relative location of modal frequencies and lead to differing acoustic impressions, such as the ombak present in the ageng lanang. In turn, changes in the structural modal frequencies relative to an acoustic wavelength create unique radiation patterns for the same modal frequencies. Disparate cavity depths, boss heights, and other properties lead to additional variations between the gongs' radiated patterns.

One difficulty in understanding gamelan gong radiation is the lack of theoretical models available to predict their behavior. While for a flat circular plate the radiation could be inferred directly from the mode shape, the gong side walls, varying shell thickness, and boss complicate their radiation characteristics. Common models, such as infinitely baffled pistons and their counterparts^{33,36,37} fail to properly account for radiation behind the gong which plays a critical role in their radiation. On the other hand, rigid spherical models, such as a vibrating cap on a sphere and their counterparts,^{33,38,39} do not have analytic solutions for non-axisymmetric radiation, severely limiting their application to only a few modes of the gong. They additionally neglect the gong's open cavity geometry. Thus, better theoretical models which can account for both the open cavity geometry and non-axisymmetric solutions would benefit radiation analysis from the gamelan gongs.

To assist future modeling and analysis of gamelan gong radiation, Ref. 40 archives directivities produced from the present work. The data set includes the far-field directivity patterns of the first fifteen modes of the ageng lanang and bebende gongs.

VI. CONCLUSIONS

The structural mode shapes of gamelan gongs often have close connections to their far-field directivity patterns. This work considered the radiation from two gongs, the ageng lanang and bebende gongs. At low-frequencies, the gongs have dipole-like radiation, while at high frequencies, the gong's become multi-directional. Modal frequency

analysis revealed that differing modal frequency values and ordering between the gongs leads to unique radiation patterns even for similar mode shapes. The gong's side walls contribute to a loss of reflectional symmetry about the gong's face's plane. Furthermore, the direction of strongest radiation is not always consistent between the two gongs.

Future work includes considering how the gong's non-linear vibrations influence its directivity and improved theoretical modeling. Other interesting areas of research could include studying directivity variations between Balinese and Javanese gamelan gongs or directivity variations between gamelan gongs and other gong-like instruments such as the tam-tam.

ACKNOWLEDGMENTS

The William James and Charlene Fuhrman Strong Family Musical Acoustics Endowed Fellowship Fund supported the corresponding author. The authors express appreciation to Dr. Jeremy Grimshaw for lending the gongs for measurement and for his insightful comments and to Joseph Avila and Ian Bacon for assistance with the measurements.

¹J. Meyer, "The sound of the orchestra," *J. Audio Eng. Soc.* **41**(4), 203–213 (1993).
²C. H. Jeong, J. G. Ih, C. H. Yeon, and C. H. Haan, "Prediction of the acoustic performance of a music hall considering the radiation characteristics of Korean traditional musical sources," *J. Korean Acoust. Soc.* **23**(2), 146–161 (2004).
³F. Otondo and J. H. Rindel, "A new method for the radiation representation of musical instruments in auralizations," *Acta Acust. Acust.* **91**, 902–906 (2005).
⁴M. C. Vigeant, L. M. Wang, and J. H. Rindel, "Investigations of orchestra auralizations using the multi-channel multi-source auralization technique," *Acta Acust. Acust.* **94**, 866–882 (2008).
⁵M. Clark and P. Minter, "Dependence of timbre on the tonal loudness produced by musical instruments," *J. Audio Eng. Soc.* **12**(1), 28–31 (1964).
⁶S. D. Bellows and T. W. Leishman, "Optimal microphone placement for single-channel sound-power spectrum estimation and reverberation effects," *J. Audio Eng. Soc.* **71**(1/2), 20–33 (2023).
⁷H. F. Olson, *Musical Engineering: An Engineering Treatment of the Interrelated Subjects of Music, Musical Instruments, Speech, Acoustics, Sound Reproduction and Hearing* (McGraw-Hill, New York, 1952).
⁸J. Pätynen and T. Lokki, "Directivities of symphony orchestra instruments," *Acta Acust. Acust.* **96**, 138–167 (2010).
⁹K. J. Bodon, "Development, evaluation, and validation of a high-resolution directivity measurement system for played musical instruments," Master's thesis, Brigham Young University, Provo, UT (2016).
¹⁰S. Weinzierl, M. Vorländer, G. Behler, F. Brinkmann, H. von Coler, E. Detzner, J. Krämer, A. Lindau, M. Pollow, F. Schulz, and N. R. Shabtai, "A database of anechoic microphone array measurements of musical instruments," Technische Universität Berlin (2017).
¹¹F. Zotter, "Analysis and synthesis of sound-radiation with spherical arrays," Doctoral dissertation, Institute of Electronic Music and Acoustics, University of Music and Performing Arts, Graz, Austria (2009).
¹²H. Ghasemi, "Directivity measurement of santur instrument," in *Proceedings of the 19th International Congress on Sound and Vibration*, Vilnius, Lithuania (2012), pp. 3120–3124.
¹³N. McLachlan, "Finite element analysis and gong acoustics," *Acoust. Aust.* **25**(3), 103–107 (1997).
¹⁴A. Varsányi, "Zur akustik des javanischen gong ageng unter berücksichtigung verwander" ("Acoustics of the Javanese gong ageng in relation to

other gong instruments"), *Beiträge Vibro- Psychoakust.* **2**(00), 1–78 (2000).
¹⁵H. Fleischer and H. Fastl, "Schwingungsuntersuchungen an gongs" ("Investigation of gong vibration"), *Beiträge Vibro- Psychoakust.* **1**(01), 1–114 (2001).
¹⁶D. W. Krueger, K. L. Gee, and J. Grimshaw, "Acoustical and vibrometry analysis of a large Balinese gamelan gong," *J. Acoust. Soc. Am.* **128**(1), EL8–EL13 (2010).
¹⁷H. Fleischer and H. Fastl, "Nichtlinearität bei gongs: Analyse des schallsignals" ("Nonlinearity of gongs: Analysis of the radiated sound"), *Beiträge Vibro- Psychoakust.* **1**(02), 1–114 (2002).
¹⁸*Ombak* is the native word for this beating phenomenon and directly translates to "wave" in English.
¹⁹R. Perrin, D. P. Elford, L. Chalmers, G. M. Swallowe, T. R. Moore, S. Hamdan, and B. J. Halkon, "Normal modes of a small gamelan gong," *J. Acoust. Soc. Am.* **136**(4), 1942–1950 (2014).
²⁰AES56-2008, *AES Standard on Acoustics: Sound Source Modeling: Loudspeaker Polar Radiation Measurements*, r2019 (Audio Engineering Society, New York, 2019).
²¹J. S. Bendat and A. G. Piersol, *Random Data: Analysis and Measurement Procedures*, 4th ed. (Wiley, Hoboken, NJ, 2010).
²²A. J. Berkhout, D. de Vries, and M. M. Boone, "A new method to acquire impulse responses in concert halls," *J. Acoust. Soc. Am.* **68**, 179–183 (1980).
²³T. W. Leishman, S. D. Bellows, C. M. Pincock, and J. K. Whiting, "High-resolution spherical directivity of live speech from a multiple-capture transfer function method," *J. Acoust. Soc. Am.* **149**(3), 1507–1523 (2021).
²⁴S. D. Bellows and T. W. Leishman, "Spherical harmonic expansions of high-resolution musical instrument directivities," *Proc. Mtgs. Acoust.* **35**, 035005 (2018).
²⁵J. R. Driscoll and D. M. Healy, "Computing Fourier transforms and convolutions on the 2-sphere," *Adv. Appl. Math.* **15**, 202–250 (1994).
²⁶A. D. Pierce, *Acoustics* (Springer International Publishing, Berlin, 2019).
²⁷R. Kennedy and P. Sadeghi, *Hilbert Space Methods in Signal Processing* (Cambridge University Press, Cambridge, 2013).
²⁸E. G. Williams, *Fourier Acoustics: Sound Radiation and Nearfield Acoustical Holography* (Academic Press, London, 1999).
²⁹T. M. Dunster, *NIST Handbook of Mathematical Functions* (Cambridge University Press, New York, 2010).
³⁰G. Weinreich, "Sound hole sum rule and the dipole moment of the violin," *J. Acoust. Soc. Am.* **77**(2), 710–718 (1985).
³¹M. S. Ureda, "Apparent apex theory," in *Audio Engineering Society Convention 61* (1978).
³²S. D. Bellows and T. W. Leishman, "Acoustic source centering of musical instrument directivities using acoustical holography," *Proc. Mtgs. Acoust.* **42**(1), 055002 (2020).
³³L. Beranek and T. Mellow, *Acoustics: Sound Fields, Transducers and Vibration*, 2nd ed. (Academic Press, New York, 2019).
³⁴S. Bellows and T. W. Leishman, "Effect of head orientation on speech directivity," in *Proceedings of Interspeech 2022* (2022), pp. 246–250.
³⁵S. D. Bellows and T. W. Leishman, "High-resolution analysis of the directivity factor and directivity index functions of human speech," in *Audio Engineering Society Convention 146* (2019).
³⁶R. M. Aarts and A. J. E. M. Janssen, "On-axis and far-field sound radiation from resilient flat and dome-shaped radiators," *J. Acoust. Soc. Am.* **125**(3), 1444–1455 (2009).
³⁷T. Mellow, "On the sound field of a resilient disk in an infinite baffle," *J. Acoust. Soc. Am.* **120**(1), 90–101 (2006).
³⁸P. M. Morse and K. U. Ingard, *Theoretical Acoustics* (Princeton University Press, Princeton, 1968).
³⁹R. M. Aarts and A. J. E. M. Janssen, "Sound radiation from a resilient spherical cap on a rigid sphere," *J. Acoust. Soc. Am.* **127**(4), 2262–2273 (2010).
⁴⁰S. D. Bellows, D. T. Harwood, K. L. Gee, and M. R. Shepherd, "Gamelan gong directivity dataset," BYU Scholars Archive, <https://scholarsarchive.byu.edu/directivity/17/> (2023) (Last viewed 14 September 2023).
⁴¹C. Touze, A. Chaigne, and O. Thomas, "Non-linear vibrations of free-edge thin spherical shells: Modal interaction rules and 1:1:2 internal resonance," *Int. J. Solids Struct.* **42**, 3339–3373 (2005).